PHYSICAL REVIEW FLUIDS **5**, 044202 (2020)

Symmetry-based nonperturbative micromanipulation in a three-dimensional microfluidic device

Jeremias Gonzalez and Bin Liu[*]
Department of Physics, University of California Merced, 5200 North Lake Rd.,
Merced, California 95343, USA

(Received 16 January 2020; accepted 1 April 2020; published 27 April 2020)

We introduce a microfluidic design that is desirable for three-dimensional (3D) micromanipulation, achieved through a set of double-layer channels with embedded symmetries. For the six-channel configuration, we show that a zero strain rate at the center of the device is protected by these symmetries, leading to a nonperturbative manipulation flow along any direction in 3D. We visualize such a nonperturbative flow structure through a finite element simulation and confirm this symmetry-protected strain-free condition. In addition to such 3D nonperturbative manipulations, we reveal two distinct perturbative flow modes available in this six-channel device, corresponding to a total of five independent modes that agrees with the degree-of-freedom counting. This symmetry-based micromanipulation is fully compatible with conventional microscopes and can be easily extended to other channel geometries for rich biological and physical applications.

DOI: 10.1103/PhysRevFluids.5.044202

I. INTRODUCTION

Symmetry becomes increasingly important in determining hydrodynamic forces at decreasing length scales. This importance results from the irrelevance of the inertia of fluids at small scales, as characterized by a vanishing Reynolds number in the Stokes regime [1]. For instance, a swimming microorganism needs to exploit nonreciprocal flow structures, e.g., via undulatory or helical motions, that avoid the stagnancy of kinematic reversibility [2]. Also, the symmetry that persists in their swimming strokes dominates the hydrodynamic interactions and synchronizations among multiple swimmers [3]. Despite this importance [4], such roles played by symmetry have been of much less concern in the design of microfluidic devices. Instead, the performance of such devices is often examined directly through computational fluid dynamics [5–7]. As another important feature arising from the negligible inertia at microscales, the net force around any suspended particles must vanish: any nonzero net force will be overdamped by the instantaneous fluid motion in the limit of the Stokes flow [2,8]. The perturbation on the suspended particles is thus only due to the finite stress associated with a nonuniform flow structure. In principle, one can utilize a uniform flow to achieve a stressless condition that leads to a surprising regime of nonperturbative manipulations of entrained particles. This regime supplements the available manipulation methodologies, including optical tweezers [9], fluid stress-based remote manipulation techniques [10,11], and their combination [12].

A generic way to realize such a nonperturbative manipulation in 3D is through three orthogonal microfluidic channels that form an intersected zone [Fig. 1(a)]. A superposition of the flow along all three axes generates a flow in any direction within this zone. Provided that such a flow is uniform (similar to that in a wind tunnel), it can be used to move suspended particles without imposing any perturbations in the Stokes regime. However, most of these designs require bulky working spaces

---

[*] bliu27@ucmerced.edu

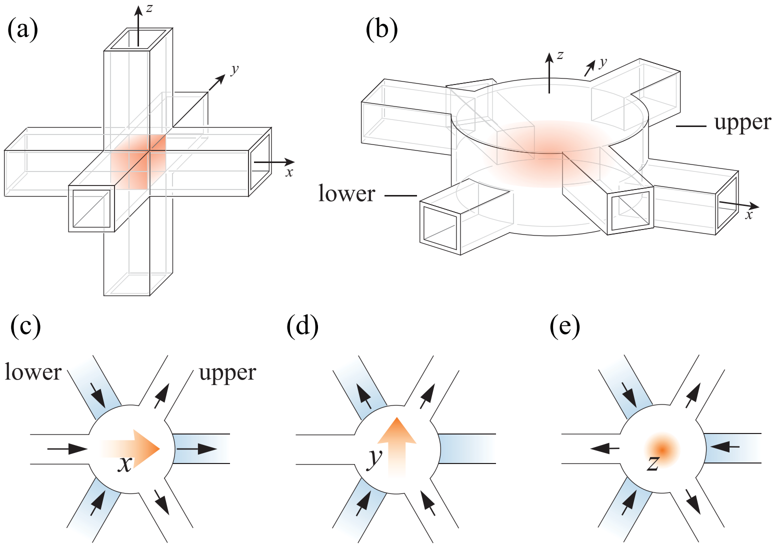

FIG. 1. Microfluidic designs for 3D nonperturbative manipulations. (a) An orthogonal-channel design allows flow generation in any direction in the intercepted volume (shaded zone), but interferes with the imaging axis. (b) A multilayer-based design of the microfluidic channels accounts for 3D flow generation in the centric region (shaded zone) and is compatible with most microscopes and imaging techniques (along the z axis). (c)–(e) Three different sets of input flows in the multilayer channels (upper: white; lower: blue) leads to three orthogonal flows (orange markers) along the x, y, and z axes, respectively.

associated with the 3D alignments of the microfluidic channels [13–15]. Such design limits their applications to nonperturbative micromanipulations, especially to those requiring high spatial and temporal resolutions.

Here, we show a symmetry-based approach to design a 3D nonperturbative manipulation chip that is compatible with most microscopes and microscale imaging techniques. Different from the aforementioned orthogonal-channel design, the 3D flow generation is achieved by incorporating multiple layers of microfluidic channels [Fig. 1(b)], which introduce an additional dimension in flow controls. The six channels in our present work lie in the x-y plane, intercepted in a center chamber. Relegation of the channels away from the z axis makes it fully compatible with most conventional microscopes. As the relatively trivial cases, an x- or y-direction flow can be generated by flushing the fluid in all layers along the x or y axis, respectively [Figs. 1(c) and 1(d)]. To generate an upward z flow (perpendicular to the x-y plane), flows are converging in all lower channels and diverging in all upper channels, leading to an upwelling net flux [Fig. 1(e)]. In addition to the generation of flows in any direction, we show both analytically and numerically that the symmetry persisting in the channel geometry and the controlling flow patterns guarantees a zero strain rate at the center of the chip, corresponding to 3D nonperturbative manipulations. We also show that the above strain rate can be manipulated by using the extra degrees of freedom that are available from the design, leading to richer microfluidic applications.

II. SYMMETRY-BASED DESIGN OF 3D MICROFLUIDIC MANIPULATIONS

We explicitly choose the above six-channel design for useful symmetries, which is sufficient for maintaining a zero strain rate at the center of the device. Here, we consider a 3D rate of strain tensor

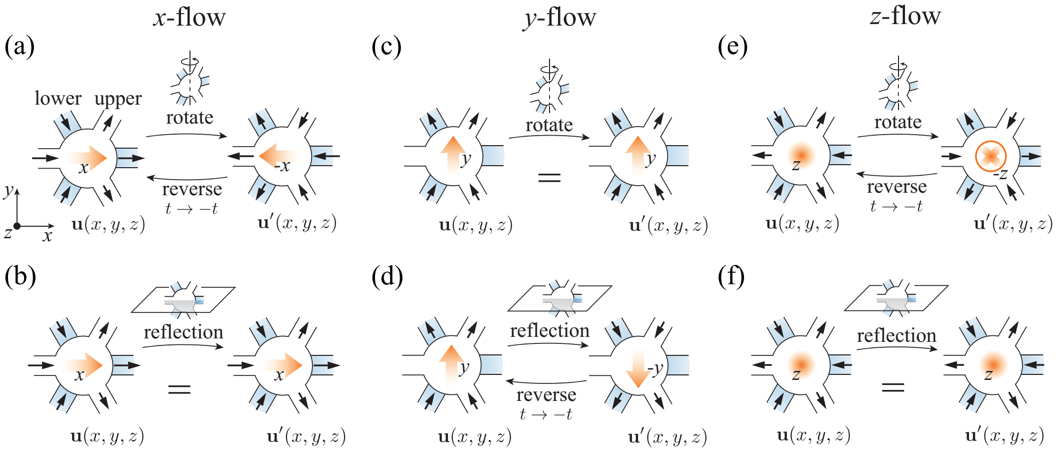

FIG. 2. Symmetry in the six-channel 3D microfluidic device. (a) In the x-flow mode, a rotation transformation of 180° about the y axis leads to a reversed velocity field, which can be canceled by a time reversal. (b) The x-flow mode also contains a reflection symmetry about the $y = 0$ plane. (c) In the y-flow mode, a rotation transformation of 180° about the y axis leads to an identical velocity field. (d) In the y-flow mode, a reflection transformation about the $y = 0$ plane leads to a reversed velocity field, which can be canceled by a time reversal. (e) and (f) The z-flow mode and the x-flow mode contain the same symmetries, shown in (a) and (b).

$\dot{\boldsymbol{\gamma}}$ at the center of the chamber $\mathbf{r} = (x, y, z) = (0, 0, 0)$ defined as [1]

$$\dot{\boldsymbol{\gamma}}|_{(0,0,0)} = \left.\begin{pmatrix} \frac{\partial u}{\partial x} & \frac{1}{2}\left(\frac{\partial u}{\partial y} + \frac{\partial v}{\partial x}\right) & \frac{1}{2}\left(\frac{\partial u}{\partial z} + \frac{\partial w}{\partial x}\right) \\ \frac{1}{2}\left(\frac{\partial u}{\partial y} + \frac{\partial v}{\partial x}\right) & \frac{\partial v}{\partial y} & \frac{1}{2}\left(\frac{\partial v}{\partial z} + \frac{\partial w}{\partial y}\right) \\ \frac{1}{2}\left(\frac{\partial u}{\partial z} + \frac{\partial w}{\partial x}\right) & \frac{1}{2}\left(\frac{\partial v}{\partial z} + \frac{\partial w}{\partial y}\right) & \frac{\partial w}{\partial z} \end{pmatrix}\right|_{(0,0,0)}, \tag{1}$$

where $\mathbf{u} = (u, v, w)$ is the flow velocity. The symmetries persistent in all three orthogonal (x-, y-, and z-) flow modes are illustrated in Fig. 2.

For the case of the x-flow mode [Fig. 1(c)], we consider a sequence of linear transformations to determine the symmetries of the flow velocity. Setting up our coordinate system relative to the center of the chamber, we take the original configuration and rotate the flow about the y axis by 180° [Fig. 2(a)]. The velocity after this transformation becomes

$$\mathbf{u}'(x, y, z) = [-u(-x, y, -z), v(-x, y, -z), -w(-x, y, -z)]. \tag{2}$$

As shown in Fig. 2(a), such a transformation simply leads to a reverse of the velocity field. As a consequence, this velocity [Eq. (2)] can be restored to the original one by applying a time reversal as

$$-\mathbf{u}'(x, y, z) = [u(x, y, z), v(x, y, z), w(x, y, z)]. \tag{3}$$

This pair of identities leads to one set of symmetries of the velocity field in the x-flow mode, i.e.,

$$\begin{aligned} u(x, y, z) &= u(-x, y, -z), \\ v(x, y, z) &= -v(-x, y, -z), \\ w(x, y, z) &= w(-x, y, -z). \end{aligned} \tag{4}$$

Also, considering the reflection symmetry of the configuration across the $y = 0$ plane [Fig. 2(b)], we obtain another set of symmetries of the velocity, i.e.,

$$\begin{aligned} u(x, y, z) &= u(x, -y, z), \\ v(x, y, z) &= -v(x, -y, z), \\ w(x, y, z) &= w(x, -y, z). \end{aligned} \tag{5}$$

With these two sets of symmetries persistent in the velocity field, we determine that all components of the rate of strain tensor vanish at the center of the geometry [$\mathbf{r} = (0, 0, 0)$]. For instance, the first identity in Eq. (4) leads to $u(x, 0, 0) = u(-x, 0, 0)$ along the x axis, giving rise to a vanishing $\frac{\partial u}{\partial x}|_{(0,0,0)}$ at the center. Also, the second identity in Eq. (4) can be written as $v(0, y, 0) = -v(0, y, 0)$ along the y axis, giving rise to a null $v(0, y, 0)$, and thus a vanishing $\frac{\partial v}{\partial y}|_{(0,y,0)}$ along the y axis. All other components of the rate of strain tensor can be determined in the same fashion. After all, the result leads to a null tensor $\dot{\boldsymbol{\gamma}}|_{(0,0,0)} = 0$.

For the case of the y-flow mode [Fig. 1(d)], we again consider a sequence of transformations to determine the symmetries of the flow velocity. Taking the original configuration, we rotate the flow about the y axis by 180° [Fig. 2(c)]. The velocity after the transformation becomes

$$\mathbf{u}'(x, y, z) = [-u(-x, y, -z), v(-x, y, -z), -w(-x, y, -z)]. \tag{6}$$

As shown in Fig. 2(c), such a transformation simply leads to the original velocity field. This identity leads to a set of symmetries of the velocity field in the y-flow mode, i.e.,

$$\begin{aligned} u(x, y, z) &= -u(-x, y, -z), \\ v(x, y, z) &= v(-x, y, -z), \\ w(x, y, z) &= -w(-x, y, -z). \end{aligned} \tag{7}$$

Next, taking the original configuration we mirror the flow about the $y = 0$ plane [Fig. 2(d)]. The velocity after the transformation becomes

$$\mathbf{u}' = [u(x, -y, z), -v(x, -y, z), w(x, -y, z)]. \tag{8}$$

As shown in Fig. 2(d), such a transformation simply leads to a reverse of the velocity field. As a consequence, this velocity can be restored to the original one by applying a time reversal as

$$-\mathbf{u}'(x, y, z) = [u(x, y, z), v(x, y, z), w(x, y, z)]. \tag{9}$$

This pair of identities leads to a set of symmetries of the velocity field in the y-flow mode, i.e.,

$$\begin{aligned} u(x, y, z) &= -u(x, -y, z), \\ v(x, y, z) &= v(x, -y, z), \\ w(x, y, z) &= -w(x, -y, z). \end{aligned} \tag{10}$$

As before, these relations show that all components of the rate of strain tensor go to 0 at the center, i.e., $\dot{\boldsymbol{\gamma}}|_{(0,0,0)} = 0$. Finally, the same set of symmetries of the x-flow mode apply to the z-flow mode [Fig. 1(e)], and thus give rise to the same zero rate of strain tensor at the center [Figs. 2(e) and 2(f)].

III. NUMERICAL SIMULATIONS OF 3D NONPERTURBATIVE MANIPULATIONS

To validate the above three modes of manipulation in an actual device, we perform a 3D simulation of the flow field in the six-channel microfluidic chip by solving an incompressible Stokes equation via the finite-element method (FEM),

$$\begin{aligned} \nabla^2\mathbf{u} - \nabla p &= \mathbf{0}, \\ \nabla \cdot \mathbf{u} &= 0, \end{aligned} \tag{11}$$

where p is the fluid pressure.

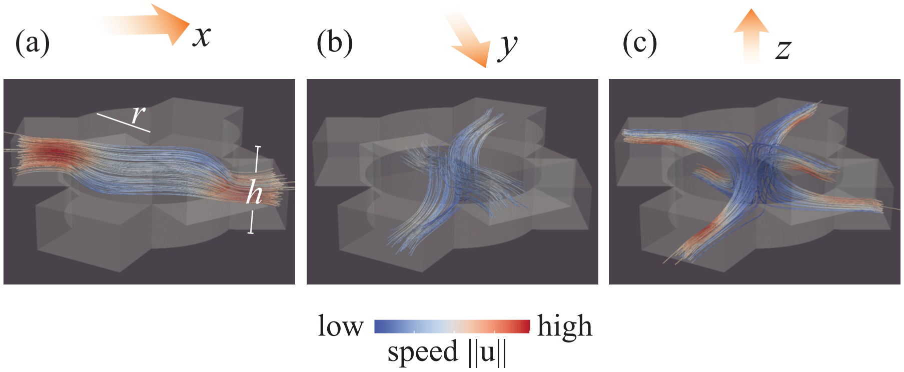

FIG. 3. The velocity fields of the three orthogonal flow modes from the finite-element simulation. (a)–(c) The characteristic streamlines (colored in flow speed) are shown for x-, y-, and z-flow modes, respectively. Here, the aspect ratio of the middle chamber $r/h = 1$.

The domain of computation is shown in Fig. 3, which is generated by Gmsh [16]. The typical mesh size here is 1/25 of the chamber radius r, corresponding to a total number of mesh points up to 4×10^4 vertices among 2×10^4 tetrahedra. For simplicity, a uniform boundary velocity $\mathbf{u}_b$ is prescribed on the opening of each channel and a no-slip boundary condition is applied to all solid walls. The velocity and pressure fields are then solved by the FEM solver FreeFEM++ [17]. Figures 3(a)–3(c) show the corresponding streamlines (shown in ParaView [18]) for the x-, y-, and z-flow modes, respectively. In each of the three modes, streamlines are parallel near the center, which indicate a uniform manipulation flow along the desired axis. We note that the velocity profile quickly converges to a parabolic flow in a rectangular duct along each channel throughout all our simulations; a different choice of the velocity profile at the opening of each channel, i.e., a parabolic profile, will not alter our simulation results in the middle chamber.

To quantify the flow velocity at the center $\mathbf{u}_0$ (for any nonperturbative manipulation), we perform the numerical simulation with various radii of the middle chamber and evaluate the corresponding flow speed. Figure 4 shows the center flow speed as a function of the aspect ratio (r/h) for each mode, where r and h are the radius and height, respectively. In all three modes, the center flow speed $\|\mathbf{u}_0\|$ (as normalized by the prescribed boundary speed at the channel opening $\|\mathbf{u}_b\|$) decreases monotonically with the increasing aspect ratio of the middle chamber. This decreasing speed compensates for the increasing cross section area (normal to the direction of the flow mode) for larger chamber radius, as required by a fixed net flux.

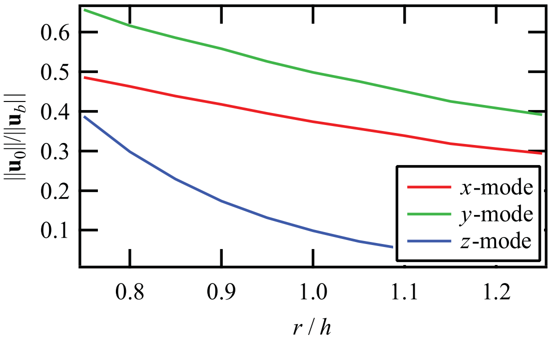

FIG. 4. The center flow speed $\|\mathbf{u}_0\|$ normalized by the prescribed speed $\|\mathbf{u}_b\|$ at the channel opening is shown as a function of the aspect ratio of the middle chamber r/h for x- (red), y- (green), and z- (blue) flow modes.

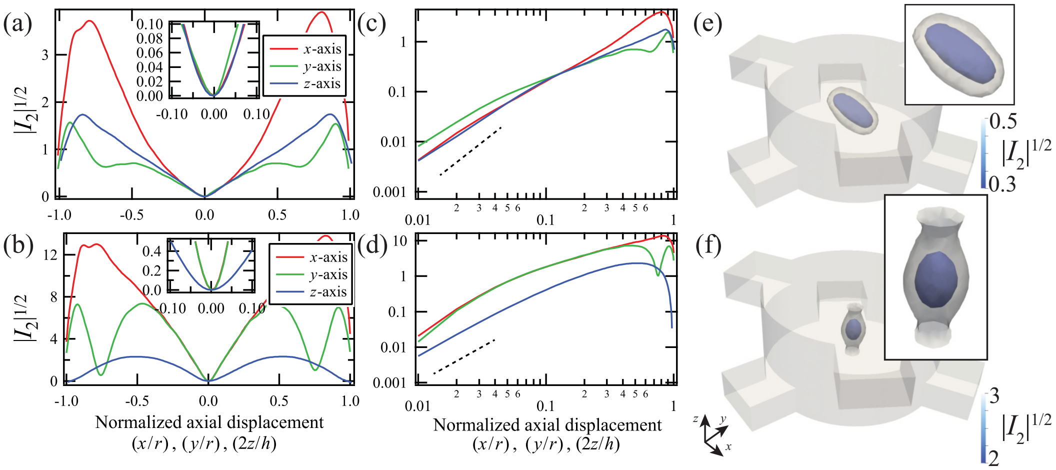

FIG. 5. Spatial distributions of the intrinsic strain rate $|I_2|^{1/2}$. (a) The distributions of $|I_2|^{1/2}$ along all axes converge to show a zero-strain region at the center in the x-flow mode (with a zoomed-in view as inset). (b) Similar convergence of $|I_2|^{1/2}$ near the center in the z-flow mode. (c) and (d) Log-log versions of (a) and (b) show a quadratic increase (indicated by the dashed lines) of $|I_2|^{1/2}$ away from the center. (e) and (f) The representative geometries of the low strain rate zones are shown in isosurfaces (with their zoomed-in views as insets) for the x- and z-flow modes, respectively.

To validate the above zero rate of strain at the center and show how it varies in space, we compute the rate of strain tensor within the entire simulation domain. Here, the rate of strain $\dot{\boldsymbol{\gamma}}$ is normalized by the characteristic speed ($\|\mathbf{u}_0\|$) and length (r), i.e., $\tilde{\dot{\boldsymbol{\gamma}}} = \dot{\boldsymbol{\gamma}} r/\|\mathbf{u}_0\|$. To avoid the complexity of tracking all six independent components of the tensor [1], we characterize the intensity of the rate of strain by its invariants (I_1, I_2, and I_3) [19] that are independent of the choice of coordinate systems,

$$I_1 = \mathrm{Tr}(\tilde{\dot{\boldsymbol{\gamma}}}), \tag{12}$$

$$I_2 = \tfrac{1}{2}\{[\mathrm{Tr}(\tilde{\dot{\boldsymbol{\gamma}}})]^2 - \mathrm{Tr}(\tilde{\dot{\boldsymbol{\gamma}}}^2)\}, \tag{13}$$

$$I_3 = \det(\tilde{\dot{\boldsymbol{\gamma}}}). \tag{14}$$

For our case where the fluid is considered incompressible, I_1 is automatically 0, and I_2 reduces to only its second term. By considering the magnitude of I_2 (I_3 behaves similarly), and taking its square root, we get a dimensionless quantity that serves as an intrinsic strain rate for assessing the quality of nonperturbation in the volume of the chamber.

Figure 5 shows this intrinsic strain rate $|I_2|^{1/2}$ in the representative x- and z-flow modes. As shown in Figs. 5(a) and 5(b), I_2 is always zero at the origin (or the center of the chamber). This vanishing I_2 is consistent with the conclusion from our earlier symmetry-based arguments, where all components of the rate of strain tensor are strictly zero due to the persistent symmetries. Near this point of zero rate of strain, $|I_2|^{1/2}$ grows gradually as an approximately second order dependency on the distance from the origin [Figs. 5(c) and 5(d)]. To further characterize the geometries of these low-strain zones near the origin, we show the isosurfaces of these relatively low values of $|I_2|^{1/2}$. In the case of the x-flow mode, such an isosurface forms an oval shape with its principal axis lying in the $y = 0$ plane. In the case of the z-flow mode, this isosurface is ellipsoidlike at relatively low $|I_2|^{1/2}$, and eventually turns into a double-sided vase that connects the top and bottom boundaries of the middle chamber. Depending on the tolerance of the perturbations, such a low strain rate zone (enclosed by an isosurface of a desired $|I_2|^{1/2}$) provides a working space for effectively nonperturbative manipulations.

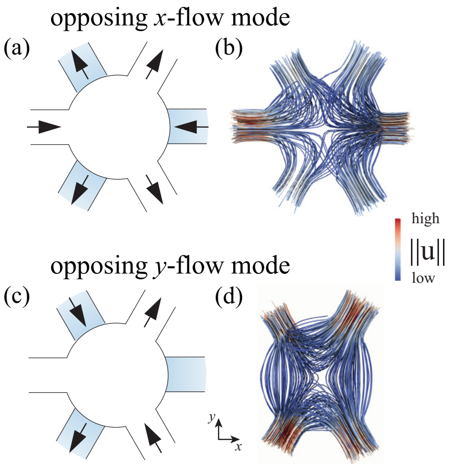

FIG. 6. Perturbative modes in the 3D six-channel microfluidic device. (a) Reversing the flows in all lower channels of the x-flow mode [Fig. 1(c)] yields a hyperbolic flow at the center of the device, as shown by the corresponding stream lines (b). (c) Reversing the flows in all lower channels of the y-flow mode [Fig. 1(d)] yields another type of hyperbolic flow that is stretched along the y axis, as shown by the corresponding stream lines (d).

IV. EXTRA DEGREES OF FREEDOM IN FLOW CONTROLS

The above three independent modes of nonperturbative manipulations in our 3D microfluidic device correspond to only three degrees of freedom in our multichannel configuration. To explore the full capacity in its 3D micromanipulation, we examine all degrees of freedom (DOF) that are available in this device. The number of DOF is, in principle, equivalent to the number of independent microfluidic channels N. Here, the six-channel configuration leads to $N = 6$ DOF by considering the fluxes through all channels to be independent. However, the conservation of fluid volume requires the fluxes from these channels to sum up to zero, which provides a constraint. This leads to the total number of DOF $= N - 1 = 5$, exceeding the three independent modes of nonperturbative manipulations corresponding to the x-, y-, and z-flow modes.

Indeed, these two additional DOF correspond to another set of flow manipulations that are embedded with nonzero strain rate at the center of the microfluidic device. Figure 6 shows these two additional perturbative modes, which can be achieved by reversing the flows in one of the two layers of the x- and y-flow modes. We term these two additional configurations the opposing x- and y-flow modes, respectively [Figs. 6(a) and 6(c)]. Figures 6(b) and 6(d) show the corresponding flow fields obtained by the FEM simulation. In both cases, the flow domains are visually split into four quadrants by the streamlines, forming a stagnation point at the center of the middle chamber.

To confirm the orthogonality between these two perturbative modes, we compare the rate of strain tensors obtained from their velocity fields. By applying symmetry arguments similar to those in the nonperturbative modes (Fig. 2), we can show that the velocity field in both cases satisfy different sets of identities.

In the opposing x-flow mode, the symmetries in the velocity lead to

$$\begin{aligned} u(x,y,z) &= -u(-x,y,-z),\\ v(x,y,z) &= v(-x,y,-z),\\ w(x,y,z) &= -w(-x,y,-z) \end{aligned} \tag{15}$$

and

$$\begin{aligned} u(x,y,z) &= u(x,-y,z),\\ v(x,y,z) &= -v(x,-y,z),\\ w(x,y,z) &= w(x,-y,z). \end{aligned} \tag{16}$$

Distinct from the nonperturbative flow modes, these identities restrict the center flow velocity to be zero, i.e., $\mathbf{u}_0 = \mathbf{0}$. Additionally, it can be easily shown that these identities give rise to a number of zero components of the rate of strain tensor at the center of the device, i.e., $\dot{\gamma}_{yz} = \dot{\gamma}_{zy} = \frac{1}{2}(\frac{\partial v}{\partial z} + \frac{\partial w}{\partial y}) = 0$ and $\dot{\gamma}_{xy} = \dot{\gamma}_{yx} = \frac{1}{2}(\frac{\partial u}{\partial y} + \frac{\partial v}{\partial x}) = 0$, while leaving the rest of the components finite.

Similarly, in the opposing y mode, the symmetries in the velocity lead to

$$\begin{aligned} u(x,y,z) &= u(-x,y,-z),\\ v(x,y,z) &= -v(-x,y,-z),\\ w(x,y,z) &= w(-x,y,-z), \end{aligned} \tag{17}$$

and

$$\begin{aligned} u(x,y,z) &= -u(x,-y,z),\\ v(x,y,z) &= v(x,-y,z),\\ w(x,y,z) &= -w(x,-y,z). \end{aligned} \tag{18}$$

In addition to a zero $\mathbf{u}_0$, these identities guarantee a distinct set of zero and nonzero components of the rate of strain tensor at the center from the opposing x mode, i.e., $\dot{\gamma}_{xz} = \dot{\gamma}_{zx} = \frac{1}{2}(\frac{\partial w}{\partial x} + \frac{\partial u}{\partial z}) = 0$, $\dot{\gamma}_{xx} = \frac{\partial u}{\partial x} = 0$, $\dot{\gamma}_{yy} = \frac{\partial v}{\partial y} = 0$, and $\dot{\gamma}_{zz} = \frac{\partial w}{\partial z} = 0$.

These distinct sets of zero components demonstrate the orthogonality between the opposing x- and opposing y-flow mode: the rate of strain tensor from one mode cannot be reproduced by the other.

To validate this orthogonality in the actual 3D device, we compute the above characteristic strain-rate components for various middle chamber geometries. As shown in Fig. 7, the normalized component $\tilde{\dot{\gamma}}_{xz}$ decreases monotonically with increasing aspect ratio of the middle chamber for the opposing x-flow mode [Fig. 7(a)] while it is consistently zero within the computational resolution for the opposing y-flow mode [Fig. 7(c)]. For the $\tilde{\dot{\gamma}}_{yz}$ component, this time the opposing y-flow mode shows a similar geometric dependency with a monotonic decrease [Fig. 7(d)], and the opposing x-flow mode is consistently zero [Fig. 7(b)]. Such binary dependencies of the rate of strain tensor on these two flow modes agree with the orthogonality predicted from the symmetry arguments. These two distinct sets of rate of strain tensor also suggests two types of perturbative manipulations that are available in this microfluidic device. Although distinct, the symmetric (corresponding to hyperbolic flows) and antisymmetric (corresponding to rotational flows) parts of the strain-rate matrix ($\boldsymbol{\nabla}\mathbf{u}$) for each mode share the same null elements as determined by symmetries, resulting in a mixture of hyperbolic and rotational flows. Therefore, the orthogonality (due to symmetry) alone cannot be used to demarcate between rotational and hyperbolic flows. We expect that such rotational and shear characteristics are determined by more details of the strain tensor, such as the eigenvalue of the symmetric part of the strain-rate tensor, together with the direction of rotation and extension (since the shear flow is a superposition of a rotational and a hyperbolic flow).

V. DISCUSSION

Our study demonstrates that the symmetries in a six-channel 3D microfluidic device can be exploited to generate desirable flow structures for nonperturbative micromanipulation. While capable of moving suspended particles along any direction in 3D (through a superposition of three orthogonal flow modes), the manipulation flow structure is endowed with a vanishing rate of strain tensor at the center of the working zone. This strain rate also grows quadratically with the distance to the center, which indicates a surprisingly uniform flow as compared to the linear dependency of

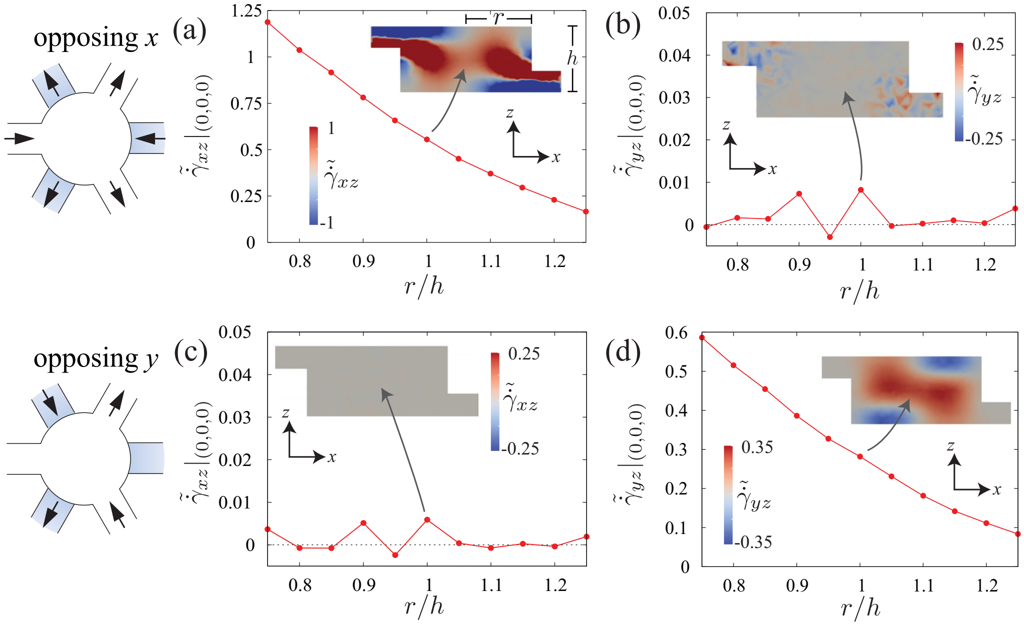

FIG. 7. Distinct strain-rate characteristics in two perturbative manipulation modes from the FEM simulations. (a) A nonzero component of the rate of strain tensor at the geometric center in the opposing x-flow mode, here $\dot{\gamma}_{xz}|_{(0,0,0)}$, is shown as a function of the aspect ratio (r/h) of the middle chamber. (b) In the same flow mode, the component $\dot{\gamma}_{yz}$ at the geometric center is consistently zero within computation resolutions. (c) The above nonzero $\dot{\gamma}_{xz}$ in the opposing x-flow mode becomes zero in the opposing y-flow mode, regardless of r/h. (d) The above zero $\dot{\gamma}_{yz}$ in the opposing x-flow mode becomes nonzero in the opposing y-flow mode, showing a similar dependency on r/h as in (a). The distribution of $\dot{\gamma}_{xz}$ and $\dot{\gamma}_{yz}$ over the $y = 0$ plane at $r/h = 1$ in each case is shown in the inset, with the apparent jumps of strain rate due to the truncated ranges of color indicators. Here, these components of rate of strain tensors are made dimensionless by normalizing $\dot{\boldsymbol{\gamma}}$ with the same factors used in the corresponding x- and y-flow modes, i.e., $\tilde{\dot{\boldsymbol{\gamma}}} = \dot{\boldsymbol{\gamma}} r/\|\mathbf{u}_0\|$.

a parabolic flow that is found in typical microfluidic transport. In addition to these nonperturbative manipulation modes, we illustrate two additional manipulation modes that are accounted for by the degree-of-freedom counting. By analyzing their symmetries, we show that these two manipulation modes are orthogonal by their rate of strain tensor. Overall, our analysis identifies all five orthogonal manipulations (three for nonperturbative and two for perturbative manipulations) in this six-channel chip, which are potentially useful for different types of microfluidic applications.

So far, only a double-layer chip has been discussed. It is expected that incorporating more layers of channels will introduce richer designs of symmetries for desired flow structures. Meanwhile, the completeness in orthogonal modes here is achieved by trying different combinations of flow directions in all channels and investigating the resultant strain rate through the presented symmetry. A more general approach is desired to recognize such orthogonal manipulation modes, especially for an arbitrary number of channels. Our success in the symmetry-based analyses suggests that a map of such a 3D multichannel device to a symmetry group may lead to all orthogonal modes directly, which will be explored in the future.

The symmetry arguments here are justified by a Stokesian Newtonian fluid. It is expected that such arguments cannot be directly applied to a non-Newtonian fluid, e.g., particle suspensions, where the time-reversal symmetry typically does not hold. For instance, this time-reversal symmetry can be easily broken by the viscoelasticity that emerges in a polymeric suspension [20,21]. However, from a perturbation-theory point of view, a symmetry-protected zero-strain rate also leads to a vanishing polymer stretch and thus a negligible polymeric stress. This implies that our nonperturbative manipulations can be potentially extended to non-Newtonian fluids, especially in the limit of a low concentration of suspended particles.

This multilayer microfluidic design is fully compatible with conventional microscopes, and can be realized by several microfabrication means [22–25]. This device can thus be applied to direct manipulation of microparticles that are sensitive to mechanical perturbations, e.g., due to a nonuniform flow [26–28]. As such, this advanced level of manipulation leads to many biophysical applications in both perturbative and nonperturbative manners.

ACKNOWLEDGMENTS

This work was supported by the National Science Foundation under Grant No. NSF CBET-1706511 and in part by the NSF-CREST: Center for Cellular and Bio-molecular Machines (CCBM) at UC Merced (HRD-1547848).

---

[1] G. K. Batchelor, *An Introduction to Fluid Dynamics* (Cambridge University Press, Cambridge, 2000).
[2] E. M. Purcell, Life at low Reynolds number, Am. J. Phys. **45**, 3 (1977).
[3] G. J. Elfring and E. Lauga, Hydrodynamic Phase Locking of Swimming Microorganisms, Phys. Rev. Lett. **103**, 088101 (2009).
[4] E. Lauga, A. D. Stroock, and H. A. Stone, Three-dimensional flows in slowly varying planar geometries, Phys. Fluids **16**, 3051 (2004).
[5] X. Xu, Z. Li, and A. Nehorai, Finite element simulations of hydrodynamic trapping in microfluidic particle-trap array systems, Biomicrofluidics **7**, 054108 (2013).
[6] P. N. Nge, C. I. Rogers, and A. T. Woolley, Advances in microfluidic materials, functions, integration, and applications, Chem. Rev. **113**, 2550 (2013).
[7] L. Capretto, W. Cheng, M. Hill, and X. Zhang, Micromixing within microfluidic devices, in *Microfluidics: Technologies and Applications*, edited by B. Lin, Topics in Current Chemistry (Springer, Berlin, Heidelberg, 2011), pp. 27–68.
[8] E. Lauga and T. R. Powers, The hydrodynamics of swimming microorganisms, Rep. Prog. Phys. **72**, 096601 (2009).
[9] K. C. Neuman and S. M. Block, Optical trapping, Rev. Sci. Instrum. **75**, 2787 (2004).
[10] T. T. Perkins, Single polymer dynamics in an elongational flow, Science **276**, 2016 (1997).
[11] A. Shenoy, C. V. Rao, and C. M. Schroeder, Stokes trap for multiplexed particle manipulation and assembly using fluidics, Proc. Natl. Acad. Sci. USA **113**, 3976 (2016).
[12] U. G. Būtaitė, G. M. Gibson, Y.-L. D. Ho, M. Taverne, J. M. Taylor, and D. B. Phillips, Indirect optical trapping using light driven micro-rotors for reconfigurable hydrodynamic manipulation, Nat. Commun. **10**, 1215 (2019).
[13] K. C. Bhargava, B. Thompson, and N. Malmstadt, Discrete elements for 3D microfluidics, Proc. Natl. Acad. Sci. USA **111**, 15013 (2014).
[14] K. Vittayarukskul and A. P. Lee, A truly Lego® -like modular microfluidics platform, J. Micromech. Microeng. **27**, 035004 (2017).
[15] S. J. Haward, C. C. Hopkins, K. Toda-Peters, and A. Q. Shen, Microfluidic analog of an opposed-jets device, Appl. Phys. Lett. **114**, 223701 (2019).
[16] C. Geuzaine and J.-F. Remacle, Gmsh: A 3-D finite element mesh generator with built-in pre- and post-processing facilities, Int. J. Numer. Methods Eng. **79**, 1309 (2009).
[17] F. Hecht, New development in freefem++, J. Numer. Math. **20**, 251 (2012).
[18] *The Visualization Handbook*, edited by C. D. Hansen and C. R. Johnson (Elsevier-Butterworth-Heinemann, Amsterdam, 2005).
[19] O. C. Zienkiewicz, R. L. Taylor, and D. Fox, *The Finite Element Method for Solid and Structural Mechanics*, 7th ed. (Elsevier-Butterworth-Heinemann, Amsterdam, 2014).

[20] A. Groisman and V. Steinberg, Elastic turbulence in a polymer solution flow, Nature (London) **405**, 53 (2000).

[21] P. E. Arratia, C. C. Thomas, J. Diorio, and J. P. Gollub, Elastic Instabilities of Polymer Solutions in Cross-Channel Flow, Phys. Rev. Lett. **96**, 144502 (2006).

[22] J. M. K. Ng, I. Gitlin, A. D. Stroock, and G. M. Whitesides, Components for integrated poly(dimethylsiloxane) microfluidic systems, Electrophoresis **23**, 3461 (2002).

[23] C.-W. Chang, Y.-J. Cheng, M. Tu, Y.-H. Chen, C.-C. Peng, W.-H. Liao, and Y.-C. Tung, A polydimethylsiloxane–polycarbonate hybrid microfluidic device capable of generating perpendicular chemical and oxygen gradients for cell culture studies, Lab Chip **14**, 3762 (2014).

[24] K. Sugioka and Y. Cheng, Femtosecond laser three-dimensional micro- and nanofabrication, Appl. Phys. Rev. **1**, 041303 (2014).

[25] H. N. Chan, Y. Chen, Y. Shu, Y. Chen, Q. Tian, and H. Wu, Direct, one-step molding of 3D-printed structures for convenient fabrication of truly 3D PDMS microfluidic chips, Microfluidics and Nanofluidics **19**, 9 (2015).

[26] G. B. Jeffery and L. N. G. Filon, The motion of ellipsoidal particles immersed in a viscous fluid, Proc. R. Soc. London, Ser. A **102**, 161 (1922).

[27] W. M. Durham, J. O. Kessler, and R. Stocker, Disruption of vertical motility by shear triggers formation of thin phytoplankton layers, Science **323**, 1067 (2009).

[28] Marcos, H. C. Fu, T. R. Powers, and R. Stocker, Bacterial rheotaxis, Proc. Natl. Acad. Sci. USA **109**, 4780 (2012).